2018-01-0739 Published 03 Apr 2018

Industrial Application of an Advanced Elliptic-Blending Turbulence Model for Wheels Aerodynamics Analysis

Michal Sumec Škoda Auto AS

Jacques Papper, Rene Devaradja, and Petr Simanek ICON Technology & Process Consulting

Pavel Růžička Evektor, spol. s r.o.

Citation: Sumec, M., Papper, J., Devaradja, R., Simanek, P. et al., "Industrial Application of an Advanced Elliptic-Blending Turbulence Model for Wheels Aerodynamics Analysis," SAE Technical Paper 2018-01-0739, 2018, doi:10.4271/2018-01-0739.

Abstract

The recent Worldwide Harmonized Light Vehicles Test Procedure (WLTP) requirements have introduced additional challenges in the car development phase. Continuous demand for environmentally friendly road vehicles has lead all OEMs to minutely investigate any potential feature that could reduce C02 emissions. Comprehension of the aerodynamics of wheels, which are one of the least explored areas, can bring novel solutions for future car designs. As the capacity of experimental facilities is limited, the need for reliable CFD methods has become crucially important. Although computational resources are continuously growing, the number of CFD simulations is increasing even faster. Professionally supported CFD process based on open-source technology has recently become an appealing alternative to commercial codes. The present paper describes a promising industrially-tested steady Reynolds Averaged Navier Stokes (RANS) approach which uses the elliptic-blending k-epsilon-zeta-f ($\zeta - f$) turbulence model [1] along with the Compound Wall Treatment [2]. The superiority of $\zeta - f$ over any other first-order RANS models resides in its capability to capture some of the near-wall anisotropic effects without any recourse to complex tailored damping functions, like in realizable k-epsilon (RKE), which are usually only valid for a defined range of flow problems. CFD optimization of the wheels in a short development cycle is described. Extensive validation of the method is presented on a set of different wheel designs with modular rims for which experimental full-scale wind tunnel data, measured in moving ground conditions, are available. Further insight into correlation of experimental static pressure from pressure strips and drag coefficient is discussed as well as relevant flow field from numerical simulations is introduced.

Introduction

With the rising demands of the European Union (EU) legislation towards decreasing the carbon dioxide (CO_2) footprint in 2020, aerodynamicists tend to put emphasis on increasingly more areas of the vehicle. The current target value of 95 g per kilometer in the WLTC cycle for the average fleet is quite challenging. As almost 25% of the aerodynamic drag of passenger cars comes from wheels and their wake interaction with the underbody and bodywork [3], this is an area of high interest. CFD can help the engineer understand the aerodynamic implications of any wheel design. A flow simulation with an enhanced turbulence model can not only predict a delta in C_D, it can also inform the aerodynamicist why that change has occurred. This makes it a powerful tool both in the early stage of development, when no physical prototypes are available for testing, as well as in the late stages when choosing between established designs.

The current study compares the C_D ranking accuracy of numerical CFD simulations with results from full scale wind tunnel experiments. The vehicles used are based on the MQB A0 modular platform. Special modular rims were used to enable the quick installation of various styling shapes. These rims consist of a core carrying structure made of steel with minimal spoke volume, as depicted in Figure 1. A stereolithographic SLA 3D printer was then used to create an insert that mounts to the core rim, representing the styling member of the modular wheel [4]. An example of modular rim with a 3D-printed insert is shown in Figure 2. Disassembly and assembly of the insert in the wind tunnel is relatively fast thanks to a central-nut that is absolutely non-invasive.

The vehicle shapes and the wheel designs are proprietary and are thus not depicted. For both types of bodywork shapes, this study incorporates wheel sizes ranging from 16″ to 18″. For the hatchback body shape, 15″ wheels are discussed as well. For the wheel designs in each load case, the aerodynamically ideal wheel (denoted as "FCR" for fully covered rim) with minimal cooling openings for the brake caliper and disc is presented as a reference. For other styling wheels, a matrix of

© 2018 SAE International. All Rights Reserved.

FIGURE 1 Modular rim without insert



© SAE International

FIGURE 2 Modular rim with the wheel insert



© SAE International

different wheel shapes is analyzed. These include different kinds of wheel covers, 5-spoke aero and normal wheels, 10-spoke aero and normal wheels, and 14-spoke wheels.

A total of 42 wheels combinations on both bodywork shapes, together with active grill shutters either closed or opened, are evaluated in this study. The CFD solver uses the elliptic-blending k-epsilon-zeta-f ($\zeta - f$) turbulence model. Experimental data were gathered at the FKFS full scale wind tunnel with the moving ground conditions and with rotating wheels. The evaluation metric in this study is primarily the C_D ranking accuracy; the ability of the CFD solver to correctly predict and rank the drag coefficient across all wheel design variations and active grill shutter configurations.

The structure of the paper runs as follows. The numerical method section discusses turbulence model, geometry modelling, boundary conditions and governing equations. Aerodynamic drag ranking accuracies for both bodyworks are presented in the Results section. Hypothesis and potential next steps are discussed in the Conclusion/Summary section.

Numerical Simulation Method

All of the numerical results presented in this paper were obtained with an iconCFD® [5] supported CFD process. A steady state incompressible turbulent flow approximation was opted to analyze the effects of different wheel designs on the overall drag coefficient (C_d) of the vehicle. Although this approach has some limitations, it generally provides satisfying relative drag predictions within reasonable computational time scales (as compared with a fully transient flow simulation).

Turbulence Model

The RANS $\zeta - f$ model, introduced by Hanjalic [1], is used in this work. This model is known to better handle turbulent wall-bounded flows (which are strongly influenced by anisotropic effects) than its parent, the standard $k - \epsilon$ model. The equations of $\zeta - f$ for an incompressible flow read

$$\nu_t = C_\mu \zeta k T$$

$$\partial_t k + U_j \partial_j k = P - \epsilon + \partial_j \left[\left(\nu + \frac{\nu_t}{\sigma_k} \right) \right] \partial_j k$$

$$\partial_t \epsilon + U_j \partial_j \epsilon = \frac{C_{\epsilon 1} P - C_{\epsilon 2} \epsilon}{T} + \partial_j \left[\left(\nu + \frac{\nu_t}{\sigma_\epsilon} \right) \partial_j \epsilon \right]$$

$$\partial_t \zeta + U_j \partial_j \zeta = f - \frac{\zeta}{k} \epsilon + \partial_j \left[\left(\nu + \frac{\nu_t}{\sigma_\zeta} \right) \partial_j \zeta \right]$$

$$L^2 \nabla^2 \mathrm{f} - \mathrm{f} = \frac{1}{T} \left(C_{f1} + C_{f2} \frac{P}{\epsilon} \right) \left(\zeta - \frac{2}{3} \right)$$

The different terms from the previous equations are k - turbulent kinetic energy; ϵ - dissipation rate of k; P - production rate of k; ζ - wall normal velocity scale; f - elliptic relaxation functi on; $L = C_L \max \left[\min \left[\frac{k^{1.5}}{\epsilon}, \frac{k^{0.5}}{\sqrt{6 C_\mu |S| \zeta}} \right], C_\eta \left(\frac{\nu^3}{\epsilon} \right)^{0.25} \right]$ - turbulent length scale; $T = \max \left[\min \left[\frac{k}{\epsilon}, \frac{0.6}{\sqrt{6 C_\mu |S| \zeta}} \right], C_\tau \left(\frac{\nu}{\epsilon} \right)^{0.5} \right]$ - turbulent time scale; $|S|$ - magnitude of strain rate tensor. The closure coefficients are given in Table 1.

TABLE 1 Closure coefficients of RANS ζ-f

$C\mu$	$C\epsilon_1$		$C\epsilon_2$	Cf_1	Cf_2
0.22	$1.4\left(1+\frac{0.012}{\zeta}\right)$		1.9	0.4	0.65
σ_k	σ_ϵ	σ_ζ	C_L	C_η	C_τ
1.0	1.3	1.2	0.36	85	6.0

© SAE International

© 2018 SAE International. All Rights Reserved.

A particularly interesting feature of the $\zeta - f$ model is its capability to physically capture potential decay of the eddy viscosity in proximity of any arbitrary wall geometry without having to resort to special damping functions that are calibrated beforehand. The decay is instead expressed as a function of the velocity scale ζ which is comparable to the wall-normal Reynold stress in the near-wall region. This important characteristic is why $\zeta - f$ was chosen in preference to another model for the present wheel design study.

With respect to grid requirements, the $\zeta - f$ model is a low Reynolds model which requires, by its nature, a fine wall-normal mesh discretization in order to resolve the whole boundary layer. Thus, the required y^+ value for such a model is less than 1 to accurately predict the near-wall flow. Because these mesh-related constraints are not easily satisfied in an industrial context, a hybrid wall treatment that combines the integration to the wall (ITW) with generalized wall functions (GWF) is incorporated into the RANS turbulence model. This method allows all y^+ values, even those falling into the critical buffer region ($5 < y^+ < 30$). In this study, the compound wall treatment (CWT) approach, proposed by Popovac et al. [2], is adopted to define the wall boundary conditions of the turbulent variables. The general form of CWT, for any flow variable ϕ, is given by:

$$\phi_P = \phi_v e^{-\Gamma} + \phi_t e^{-\frac{1}{\Gamma}}$$

The index "P" denotes the center of the wall-adjacent cell. The indices "v" and "t", respectively, stand for the viscous and turbulent contributions of ϕ. Finally, Γ represents Kader's blending coefficient. The previous decomposition is applied to the fields P, ϵ, f and ν_t as reported in Table 2. The different terms involved in the near-wall treatment are: ν_l - the laminar viscosity; y - the wall distance; $y_P^* = \frac{C_{\mu w}^{0.25} k_P^{0.5} y_P}{\nu_l}$; $C_{\mu w} = 0.07$ - the non-dimensional wall distance; $u^* = C_{\mu w}^{0.25} k^{0.5}$ - the turbulent velocity scale; κ = 0.41 - the Von Karman constant; $u_\tau = \sqrt{(\nu_l + \nu_{t,P})\frac{U_P}{y_P}}$ - the friction velocity; E = 8.3 - the log-law constant.

TABLE 2 CWT formulation for RANS ζ – f

ϕ	ϕ_v	ϕ_t	Γ
ϵ	$\frac{2\nu_l k_P}{y_P^2}$	$\frac{u_P^{*3}}{\kappa y_P}$	$0.001\frac{y_P^{*4}}{1+y_P^*}$
P	$C_\mu \zeta_P \frac{k_P^2}{\epsilon_P}\left(\frac{U_P}{y_P}\right)^2$	$\frac{u^{*2} u_\tau}{\kappa y_P}$	$0.01\frac{y_P^*}{1+5y_P^*}$
ν_t	ν_l	$\frac{\kappa u_P^* y_P}{\ln(E y_P^*)}$	
f	$-\frac{2\nu_l \zeta_P}{y_P^2}$	0	0

Modelling of Rotating Wheels

The rotation of wheels is simulated by the Moving Reference Frame (MRF) model in which the local momentum equation is formulated as follows:

$$\partial_t(\rho U) + \nabla.(\rho U_r \nabla U) = -\nabla p + \nabla.\tau_{eff} - \rho(\omega \times U)$$

Where $\boldsymbol{\omega}$ is the rotational velocity vector and $\boldsymbol{U_r}$ is the velocity relative to the moving coordinate system. The relationship between the absolute velocity $\boldsymbol{U}$, the relative position $\boldsymbol{r}$ and $\boldsymbol{U_r}$ is defined as:

$$U_r = U - \omega \times r$$

The other terms from the previous equation stand for: ρ - air density (assumed to be constant); p - pressure; τ_{eff} - effective shear stress tensor. As illustrated in Figure 3, the MRF zone (where the user-defined rotational movement is applied to a "frozen" wheel's position) encompasses the wheel's rims and the surrounding flow region. The axisymmetric tire part that is in the outer stationary mesh region is assigned a rotating wall boundary condition. The wheel pad on the wind tunnel floor is modelled as a moving wall with a prescribed tangential velocity. Surface mesh of the rim and tire is presented in Figure 4. Generated volume meshes have on average 150 million of hexadominant cells. A total of 10 layers of prisms were used to effectively refine the boundary layer adjacent to the walls. Finally, scanned tires with longitudinal grooves were utilized in all cases and all wheel sizes.

FIGURE 3 Depiction of the wheel model and MRF zone

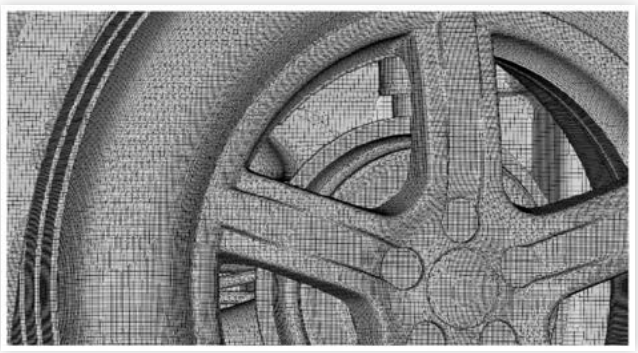


© SAE International

© SAE International

© 2018 SAE International. All Rights Reserved.

FIGURE 4 Details of the tire and rim surface mesh



© SAE International

Simulation Boundary Conditions and Specifications

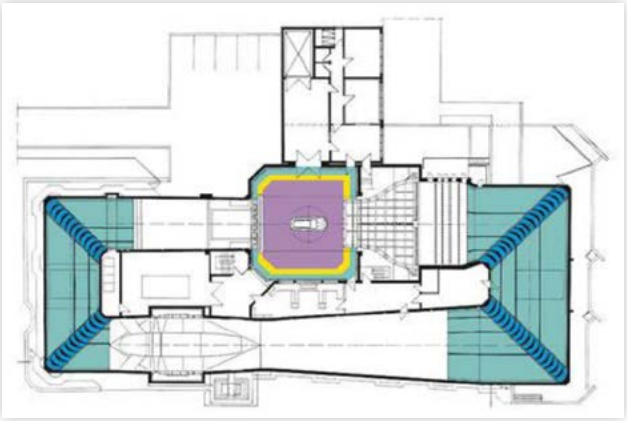
The computational box-domain had a length of approximately 15 vehicle lengths, a width of 10 vehicle widths and a height of 8 car heights. A first order upwind convection scheme was applied to all the turbulent variables and a second order upwind convection scheme was used for the momentum equation only. The mesh size was opted to maintain the suggested $y+$ values. All the cases were run on 720 CPU cores with the steady state solver for 12,000 iterations to achieve good convergence (assessed by the time plot of initial residuals and total drag coefficient). The total number of iterations and drag convergence are in agreement with previous work of Jakirlic, S., Kutej, L., Unterlechner, P., and Tropea, C. [8]. Rims were systematically positioned on the "opening" in contact patch. Calculated maximal deviation between positions on "opening" and "spoke" is $\Delta C_D \pm 0.002$.

Experimental Method

All experimental work was conducted at the FKFS aeroacoustics full-scale wind tunnel in Stuttgart, Germany (Figure 5). The wind tunnel has a horizontal routing of air flow with an open free-flow jet test section (Göttingen-type wind tunnel) in order to represent the air flow conditions of a vehicle driving on a road surface as realistically as possible. The test is simulated with turning wheels and moving ground in the wind tunnel. This is done using a 5-belt system consisting of a middle moving belt and four wheel drive units, combined with boundary layer conditioning-systems [6].

The dimensions of nozzle (width x height) are 5.8 m x 3.87 m, with the contraction ratio of 4.41 and diameter of axial fan 7.1 m. Main operating output is 3.3 MW, exit area of nozzle 22.45 m2, and length of open-nozzle test section, where full scale models are placed is 9.95 m. All tests were conducted at the free stream velocity v = 38.88 m/s, which in turn leads to the Reynolds number of $Re = 1.1x10^6$. Moving ground, suction of the boundary layer and rotating wheels were active for all runs. Vehicles were for loaded to the baseline ride height for all wheel configurations. The declared repeatability error of the wind tunnel is $\Delta C_D \pm 0.001$. Pressure data from p-strips were recorded at 10 Hz and time-averaged for interval 45 s. The free-stream dynamic and static pressures were acquired at the start of the working section. Manufacturer quoted accuracy is <10 Pa.

FIGURE 5 Schematic drawing of the FKFS full scale wind tunnel



© SAE International

Metrics

Aerodynamic drag ranking accuracy was chosen as the crucial metric for comparing numerical and experimental results. It provides a measure of the capability of the simulation tool to correctly predict the drag ranking from the aerodynamically best to the worst wheel designs. In this paper the ranking accuracy is defined as the number of correctly predicted positional rankings divided by the total number of positional ranking as in [7]. The referenced example is presented in Figure 6. "The blue bars show five sample measurements of increasing value. The red line represents the predicted values for each sample measurement. Each measurement has a rank order position relative to the other four samples, leading to a total of 20 positional rankings for this particular data set. The rank order of samples 1, 2 and 3 were correctly predicted four times. The rank order of samples 4 and 5 were correctly predicted three times. The net result is a total of 18 correctly predicted sample rank orders and a final ranking accuracy of 90%." [7]

FIGURE 6 Ranking accuracy sample [7]



© SAE International

© 2018 SAE International. All Rights Reserved.

Results

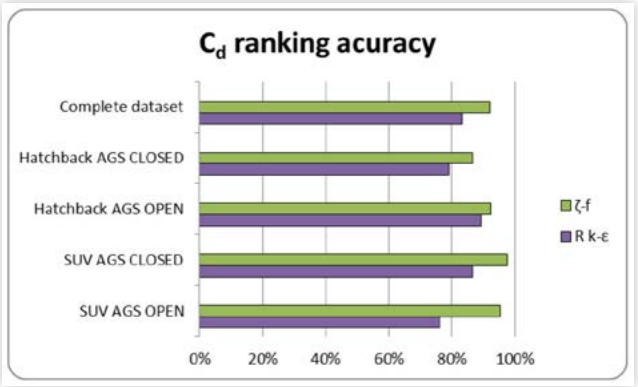
C_D Ranking Accuracy

The ranking accuracy of the complete wheel numerical dataset and for particular bodywork types and load cases is presented in Figure 7. Results are compared for $\zeta - f$ and realizable k-epsilon turbulence models with MRF approach for rotation of wheels. Whereas different number of wheels were computed for each loadcase matrix, the results for every loadcase were averaged by weighted arithmetic mean. This makes the results of each loadcase comparable.

In terms of $\zeta - f$ approach, very good ranking accuracy of 92% was achieved for the complete dataset in. The worst ranking accuracy of 87% was obtained in the hatchback cases with active grill shutter closed loadcases. One possible reason for this particular deviation could be the fact that closing the active grille shutters directs less mass flux through the wheelhouse and the rim, thus making the wheel more drag sensitive. Cases with active grill shutter opened have a ranking accuracy of 93%. Even better results were achieved in case of the SUV vehicle; for the active grill shutter closed load case, the ranking accuracy was 98%, and for the active grill shutter opened load case, the ranking accuracy was 95%. The possible reasons of different behavior between hatchback and SUV loadcases will be an object of further research, but could be hypothetically attributed to the fact that hatchback is fitted with wheels of smaller diameter whereas SUV with bigger one. Providing that both cars have the same size of the front and rear wheelhouses and SUV vehicle has higher ride height, thus leading to more filled wheelhouse with wheel. So for SUV AGS opened loadcase, air flowing through engine compartment and then through wheelhouses is more "throttled" than in hatchback AGS opened loadcases.

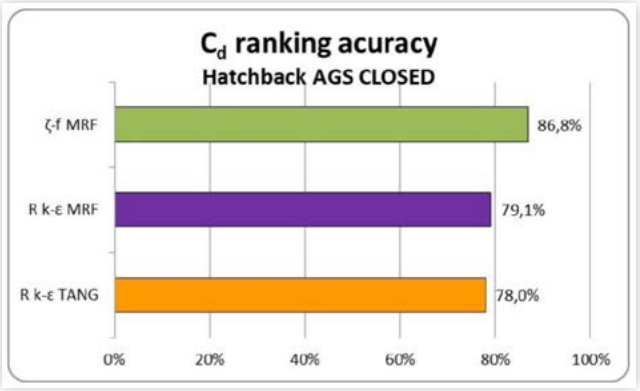
Regarding the realizable k-epsilon turbulence model, the ranking accuracy of the complete dataset has reached 83% which is in turn 9% lower accurate than for $\zeta - f$. Looking at the particular loadcases, for hatchback vehicle the difference between AGS closed and opened loadcases is analog the RKE. Namely, for AGS closed 79% and for AGS opened 89%. Similar trends are captured for the SUV bodywork. Prediction

FIGURE 7 C_D ranking accuracy for different bodywork types and active grill shutter load cases



© SAE International

FIGURE 8 C_D ranking accuracy comparing $\zeta - f$ and realizable k-ε turbulence models together with MRF and tangential velocity boundary conditions



© SAE International

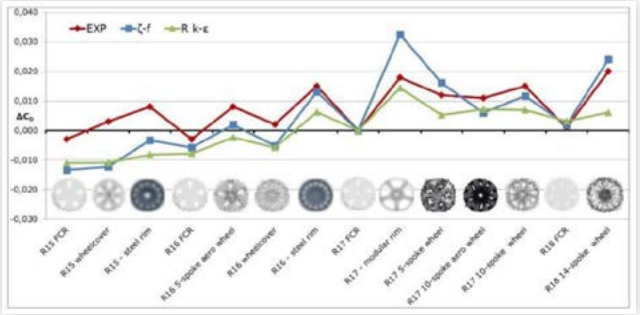
for AGS closed is peaking at the 87%, on the contrary accuracy for AGS opened is lower (76%) analog to the RKE approach. The attributable reason for such low accuracy will be subject of further future analysis. To sum up, the overall performance of $\zeta - f$ was better to RKE for both bodyworks and loadcases.

To find out whether the performance of utilized turbulence model is due to additional normalized wall-normal velocity scale ζ and elliptic relaxation function f or due to MRF rotational approach, the Figure 8 shows comparison between the MRF and tangential velocity boundary condition. Tangential velocity is applied on both the rim and tire and the reference is the experimental result from hatchback AGS closed loadcase. It is obvious that the difference between MRF and tangential velocity approach at realizable k-epsilon turbulence model simulations is just 1.1%, whereby delta between $\zeta - f$ and realizable k-epsilon with MRF is more than 7%.

Relative Correlation Of ΔC_D

Hatchback The correlation of the numerical and experimental values for cases with closed active grill shutter are presented in Figure 9. This data set consists of 14 total wheels. The reference wheel is the 17″ fully covered rim (FCR), to

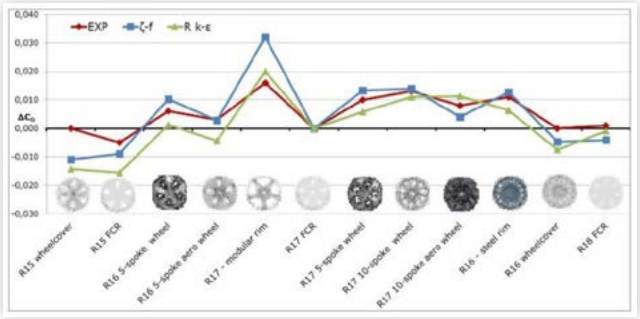
FIGURE 9 Hatchback - C_D correlation for loadcase AGS closed



© SAE International

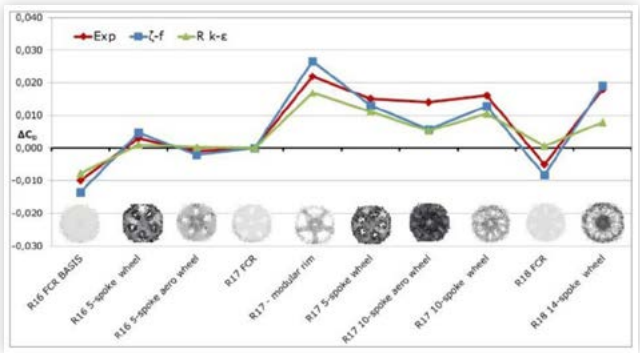
© 2018 SAE International. All Rights Reserved.

FIGURE 10 Hatchback - c_D correlation for loadcase AGS open



© SAE International

FIGURE 11 SUV - C_D correlation for loadcase AGS closed



© SAE International

which all measured wheels were compared. The wheel matrix is ordered on the *x-axis* according the wheel size, from 15″ to 18″. On the *y-axis* the relative difference from the reference wheel in drag counts is shown. The red line represents the experimental data, the blue line shows data from $\zeta - f$ and green line depicts RKE computation.

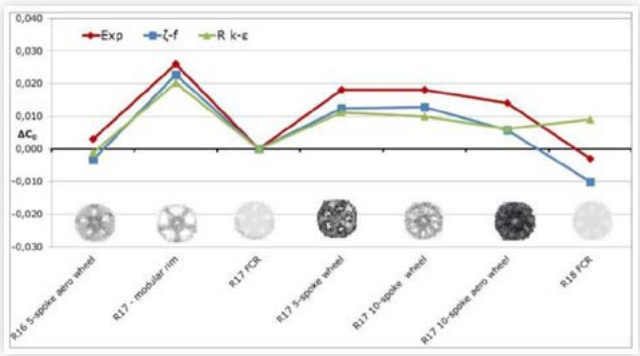
Both numerical trend lines correlate in a satisfactory manner. The least correlated are the 15 inch wheels, which are systematically underpredicted by almost 10 drag counts ($\zeta - f$ performs better for 15 inch steel rim), and the 17 modular rims, which are overpredicted by 20 counts in $\zeta - f$. By contrast, RKE performs better for this wheel but shows worse prediction for 18 inch 14-spoke design. In general, all other wheel designs show the drag difference deviation to within 5 counts for $\zeta - f$, eventually 10 counts for k-epsilon. The fully covered rims prediction is better for bigger wheels (both turbulence models) but worse for 15 and 16 inch wheels. The experimental dispersion of the design space between 15 inch FCR and 18 inch 14-spoke rim is 23 drag counts, compared to $\zeta - f$ prediction of 37 counts and RKE 17 counts.

Results for the active grill shutter open are presented in Figure 10. For this loadcase a limited matrix of 12 wheels was utilized. The reference wheel for this dataset is the 17 rim FCR. Analogously to the previous loadcase, the red line represents experimental data, blue line depicts $\zeta - f$ and green RKE.

Similar drag deviations and trends are visible in comparison to the closed AGS state. The 17″ modular wheel seems to be overpredicted systematically by $\zeta - f$, by approximately 20 drag counts in this dataset. RKE is performing better at this particular wheel but showing greater deviation at 15 inch wheels. The global numerical trend line otherwise correlates well for both approaches with the experimental data. The fully covered rims also indicate good overall agreement with the experimental values except previously mentioned 15 inch. Experimental dispersion of the design space between the 15 inch FCR and the 17 inch modular rim is 21 counts, compared to $\zeta - f$ prediction of 41 counts and k-epsilon 36 counts.

SUV The correlation of the numerical and experimental values for SUV cases with closed active grill shutters are presented in Figure 11. Measured and simulated wheel datasets consist of 10 different wheel designs referenced to the 17 inch FCR. The SUV vehicle baseline ride height is approximately 100 mm higher than hatchback vehicle. The 15 inch wheels were not included, as the vehicle is only fitted with wheels in the range of 16 inch to 18 inch.

FIGURE 12 SUV - C_D correlation for load case AGS open



© SAE International

Good overall agreement of numerical data with experimental data is evident. Interestingly, the 17 inch modular rim shows better results in $\zeta - f$ than with the hatchback type bodywork, despite the fact that it is mildly overpredicted. The majority of the drag difference is numerically slightly overpredicted, with the exception of the 17 inch 10-spoke aero wheel. RKE fails with the 18 inch 14-spoke rim prediction analog to the hatchback loadcase. Experimental dispersion of the design space between 16 inch FCR and 17 inch modular rim is 32 drag counts, which is 11 counts more than for hatchback loadcase. Numerical dispersion for $\zeta - f$ is 41 drag counts, for RKE 25 counts.

Results for the active grill shutter open are presented in Figure 12. For this load case, a limited range of 7 wheels was experimentally measured. Good agreement is achieved for all datasets. The reference wheel here is the 17 inch FCR.

In comparison to the AGS closed load case, the 17 inch modular rim shows a bit better agreement, with a deviation of 3 drag counts in case of $\zeta - f$ (RKE 6 counts). The performance of the RKE is aggravated by the 18 inch FCR where the deviation accounts for 12 drag counts. The experimental dispersion of the design space between the 18 inch FCR and the 17 inch modular rim is 29 counts, which is 15 counts more than for the hatchback case. Numerical dispersion for $\zeta - f$ is 36 drag counts, for RKE 21 counts.

© 2018 SAE International. All Rights Reserved.

Assessment of Static Pressure Coefficient C_p and Flow Field

To better understand the experimental coherence between reducing drag coefficient of the various wheel configurations and the mechanisms in the flow field, static pressure coefficient C_P from pressure strips was considered and assessed. Pressure strips were installed on the most aerodynamically interesting spots all around the vehicle. As stated by the Evrard, Cadot, Herbert, Ricot, Vigneron [10], 90% the bluff body's aerodynamic drag is generated by the separation at the base and the ability of the mixing layer to retain the base pressure recovery.

The static pressure C_P at the base symmetry at the height of the rear window correlated to the measured drag coefficient is visualized in the Figure 13. The experimental matrix consist of approximately 30 wheels of different designs and sizes for hatchback loadcase with AGS closed. Dashed lined depicts the linear fit of measured set and dots in the green dashed line are wheels with best drag among the matrix. It is evident that they tend to lower suction at the base retaining the best base pressure recovery and consequently the smallest wake recirculation area behind the vehicle.

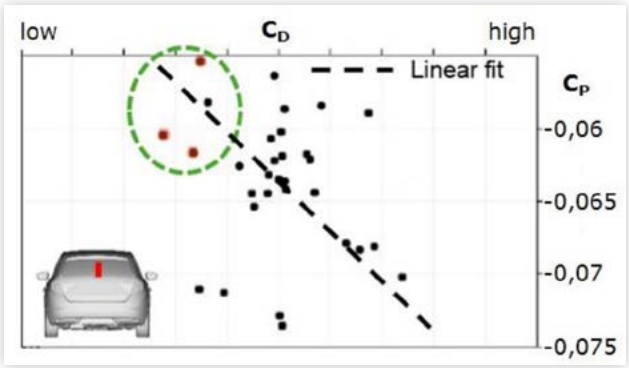
This is further reinforced and confirmed by the normalized velocity magnitude from $\zeta - f$ numerical simulation in plane $x = 4000\ mm$ presented in Figure 14. Two wheels are contrasted, 15 inch fully covered rim and 18 inch 14-spoke wheel. These two create maximal dispersion for the given dataset loadcase. Substantial wake is evident behind the rear wheels affecting the suction and the base pressure recovery at the aft of the vehicle. Despite the fact that the difference in the flow field seems to be enormous, the delta in the static pressure on the base is $\Delta C_p = -0.015$. Computed difference in terms of drag coefficient C_D between them is 37 counts.

Another area that justifies variations in the flow field is behind front left wheel, located at the height of the wheel center (Figure 15). Analogically to the static pressure at the base of the square back vehicle, common factor for the less "draggy" wheel sets are the higher values where the intrinsic recirculation region from the front wheel is anticipated. Looking at the 15 inch FCR and 18 inch 14-spoke wheel, the static pressure dispersion is $\Delta C_p = 0.033$. This is 0.018 more than recorded at the base for both configurations. Nevertheless it could not be directly compared, this leads to conviction that recirculation region of front wheels contribute by a great deal to the overall drag.

Last node to be assessed is the in the vehicle symmetry line (Figure 16) at the underbody engine panel. Nevertheless it is located upstream from the front wheels, relatively notable changes in static pressure were observed.

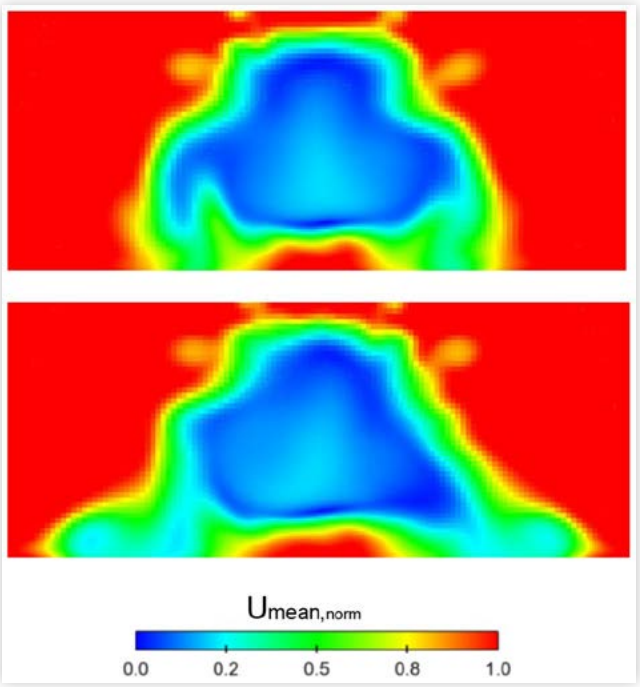
Static pressure dispersion between the 15 inch FCR and 18 inch 14-spoke wheel is $\Delta C_p = 0.052$, which is the biggest difference among three monitored areas. Wheels with the best total drag coefficient correlate well at higher spectrum of the pressure. This once again indicates smaller wake region downstream from the lower part of the front bumper towards front wheels. Clarification of the driving mechanism behind this behavior will be topic of the next studies and analyses.

FIGURE 13 Correlation between C_D and C_p at the vehicle base for various wheels, —-- dashed line represents linear fit



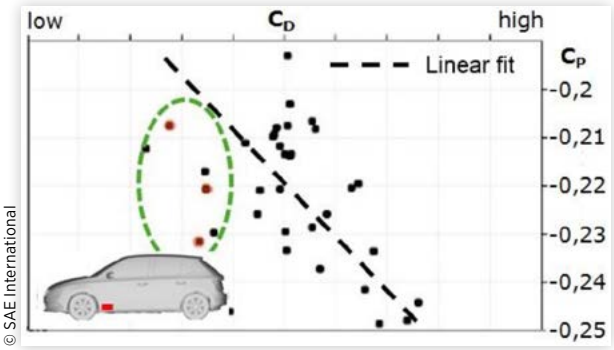
© SAE International

FIGURE 14 Normalized mean velocity magnitude in plane x = 4000 m for 15 inch FCR (above) and 17 inch modular rim (below) wheels



© SAE International

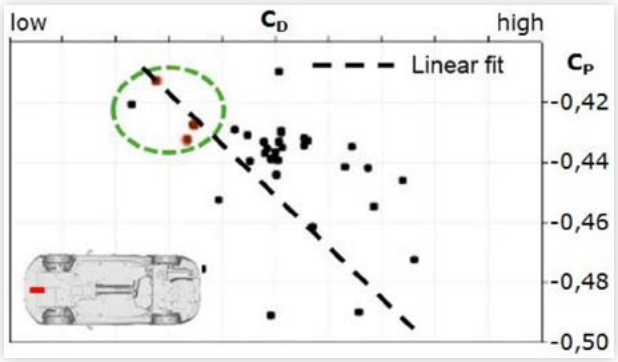
FIGURE 15 Correlation between C_D and C_p behind front left wheel for various wheels, —-- dashed line represents linear fit



© SAE International

© 2018 SAE International. All Rights Reserved.

FIGURE 16 Correlation between C_d and C_p behind front left wheel for various wheels, –-- dashed line represents linear fit



© SAE International

Summary and Conclusions

A matrix of 42 wheel combinations on two bodywork shapes together with loadcase of active grill shutters either closed or opened were evaluated in this study in both numerical ($\zeta - f$ and realizable k-epsilon turbulence models) and experimental conditions.

Drag coefficient improvements or deteriorations for each configuration were evaluated utilizing the ranking accuracy metric. $\zeta - f$ results achieved accuracy of 92%, with worst value of 87% for hatchback AGS closed loadcase. On the other hand, RKE reached 83% overall and the worst prediction achieved 76% for SUV AGS opened loadcase. Performance of both turbulence model approaches in conjunction with either MRF or tangential velocity boundary condition on hatchback AGS closed loadcase was assessed. $\zeta - f$ was responsible for improvement of 7,7% against RKE, however implementation of the MRF fell short in improvement of just 1.1% in comparison with tangential velocity boundary condition. It was shown that the correlation of numerical prediction to experimental values is function of mass flux flowing through the wheelhouse and the rim for different bodyworks and ride heights. Overall, $\zeta - f$ turbulence model has shown very good agreement in this particular industrial application, with satisfactory general trendlines across the range of various wheels sizes and designs. Following this work, joint effort of Škoda Auto and ICON on further improvement of $\zeta - f$ turbulence model implementation in iconCFD® has significantly reduced the number of iterations required to achieve a converged solution. Current methodology requires an order of magnitude less in number of iterations to achieve the same results.

Modular wheel approach has been shown to be a feasible experimental method for aerodynamic development of various wheel stylings. Synergy between CFD and wind tunnel experiments is crucial and necessary, as results have shown. Correlation between experimental static pressure from the p-strips at the base of the vehicle and drag coefficient showed the tendency of reducing the recirculation region behind the vehicle thus improving base pressure recovery. Similar trends were observed behind the front left wheel and on the engine underbody panel where the mechanism is not fully understood and will be a topic of future work.

Other possible next steps would include the implementation and critical assessment of the RBM method (sliding mesh), together with some transient scale-resolving turbulence model. Evaluation of the vehicle lift is part of the long term ambitions in correlating experimental and numerical results.

Acknowledgements

The authors would like to gratefully acknowledge the support and contribution from the Aerodynamics Team at Škoda Auto, Mladá Boleslav, Czech Republic, especially Mr. Vlastimil Hörzenberger and Mr. Jakub Filipský. The authors would also like to thank Škoda Auto for giving their permission to publish this paper.

References

1. Hanjalic, K., Popovac, M., and Hadziabdic, M., "A Robust near-Wall Elliptic-Relaxation Eddy-Viscosity Turbulence Model for CFD," *International Journal of Heat and Fluid Flow* 25:1047-1051, 2004.
2. Popovac, M. and Hanjalic, K., "Compound Wall Treatment for RANS Computation of Complex Turbulent Flows and Heat Transfer," *Flow Turbulence Combust* 78:177-202, 2007.
3. Hucho, W.H., "*Aerodynamics of Road Vehicles*," (Society of Automotive Engineers, Inc., 1998).
4. Vdovin, A., "Investigation of Aerodynamic Resistance of Rotating Wheels on Passenger Cars," Thesis for the Degree of Licentiate of Engineering, Chalmers University of Technology, Gothenburg, 2013.
5. http://www.iconcfd.com/, 12 Nov 2017.
6. http://www.fkfs.de/en/automotive-engineering/leistungen/wind-tunnels/vehicle-aeroacoustics-wind-tunnel/technical-data/, 12 Nov 2017.
7. Lietz, R., Larson, L., Bachant, P., Goldstein, J. et al., "An Extensive Validation of an Open Source Based Solution for Automobile External Aerodynamics," SAE Technical Paper 2017-01-1524, 2017, doi:10.4271/2017-01-1524.
8. Jakirlic, S., Kutej, L., Unterlechner, P., and Tropea, C., "Critical Assessment of some Popular Scale-Resolving Turbulence Models for Vehicle Aerodynamics," *SAE Int. J. Passenger Cars - Mech. Syst.* 10(1):235-250, 2017, doi:10.4271/2017-01-1532.
9. Jakirlic, S., Kutej, L., Basara, B., and Tropea, C., "Computational Study of the Aerodynamics of a Realistic Car Model by Means of RANS and Hybrid RANS/LES Approaches," *SAE Int. J. Passeng. Cars - Mech. Syst.* 7(2):559-574, 2014, 2014, doi:10.4271/2014-01-0594.
10. Evrard, A., Cadot, O., Herbert, V., Ricot, D. et al., "Fluid Force and Symmetry Breaking Modes of a 3D Bluff Body with a Base Cavity," *Journal of Fluids and Structures*, Elsevier 61:99-114, 2016.

All rights reserved. No part of this publication may be reproduced, stored in a retrieval system, or transmitted, in any form or by any means, electronic, mechanical, photocopying, recording, or otherwise, without the prior written permission of the copyright holder.

Positions and opinions advanced in this paper are those of the author(s) and not necessarily those of SAE International. The author is solely responsible for the content of the paper.

ISSN 0148-7191